

Hole weak anti-localization in a strained-Ge surface quantum well

R. Mizokuchi, P. Torresani, R. Maurand, Z. Zeng, Y.-M. Niquet, M. Myronov, and S. De Franceschi

Citation: *Appl. Phys. Lett.* **111**, 063102 (2017); doi: 10.1063/1.4997411

View online: <http://dx.doi.org/10.1063/1.4997411>

View Table of Contents: <http://aip.scitation.org/toc/apl/111/6>

Published by the [American Institute of Physics](#)

Articles you may be interested in

[Anomalous tunneling characteristic of Weyl semimetals with tilted energy dispersion](#)

Applied Physics Letters **111**, 063101 (2017); 10.1063/1.4997296

[Degradation-induced low frequency noise and deep traps in GaN/InGaN near-UV LEDs](#)

Applied Physics Letters **111**, 062103 (2017); 10.1063/1.4985190

[Optically active dilute-antimonide III-nitride nanostructures for optoelectronic devices](#)

Applied Physics Letters **111**, 061101 (2017); 10.1063/1.4997450

[Controllable cracking behavior in Si/Si_{0.70}Ge_{0.30}/Si heterostructure by tuning the H⁺ implantation energy](#)

Applied Physics Letters **111**, 062104 (2017); 10.1063/1.4996892

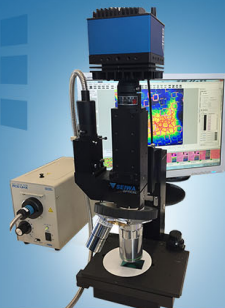
[Effect of oxygen plasma on nanomechanical silicon nitride resonators](#)

Applied Physics Letters **111**, 063103 (2017); 10.1063/1.4989775

[Tunable thermal conductivity in mesoporous silicon by slight porosity change](#)

Applied Physics Letters **111**, 063104 (2017); 10.1063/1.4997747

 **SEIWA**
OPTICAL



NEW IR-2200 Microscope

For fast performance and high precision measurements

[LEARN MORE](#) 

Hole weak anti-localization in a strained-Ge surface quantum well

R. Mizokuchi,^{1,2} P. Torresani,^{1,2} R. Maurand,^{1,2} Z. Zeng,^{2,3} Y.-M. Niquet,^{2,3} M. Myronov,⁴ and S. De Franceschi^{1,2,a)}

¹CEA, INAC-PHELIQS, F-38000 Grenoble, France

²University Grenoble Alpes, F-38000 Grenoble, France

³CEA, INAC-MEM, F-38000 Grenoble, France

⁴Department of Physics, University of Warwick, Coventry CV4 7AL, United Kingdom

(Received 12 April 2017; accepted 8 July 2017; published online 8 August 2017)

We report a magneto-transport study of a two-dimensional hole gas confined to a strained Ge quantum well grown on a relaxed Si_{0.2}Ge_{0.8} virtual substrate. The conductivity of the hole gas measured as a function of a perpendicular magnetic field exhibits a zero-field peak resulting from weak anti-localization. The peak develops and becomes stronger upon increasing the hole density by means of a top gate electrode. This behavior is consistent with a Rashba-type spin-orbit coupling whose strength is proportional to the perpendicular electric field and hence to the carrier density. In the low-density, the single-subband regime, by fitting the weak anti-localization peak to an analytic model, we extract the characteristic transport time scales and a spin splitting energy $\Delta_{SO} \sim 1$ meV. Tight-binding calculations show that Δ_{SO} is dominated by a cubic term in the in-plane wave vector. Finally, we observe a weak anti-localization peak also for magnetic fields parallel to the quantum well and associate this finding to an effect of intersubband scattering induced by interface defects.

Published by AIP Publishing. [<http://dx.doi.org/10.1063/1.4997411>]

Holes in p-type SiGe-based heterostructures are promising candidates for quantum spintronic applications.^{1,2} They are expected to display a relatively small in-plane effective mass,^{3,4} favoring lateral confinement, as well as long spin coherence times, stemming from a reduced hyperfine coupling (natural Ge is predominantly constituted of isotopes with zero nuclear spin and holes are less coupled to nuclear spins due to the p-wave symmetry of their Bloch states⁵). In addition, low-dimensional, SiGe-based structures benefit from a strong and electrically tunable spin-orbit (SO) coupling.^{4,6–10} This property could be exploited to achieve purely electric spin control^{11,12} which is desirable for spintronic applications such as spin field effect transistors,^{13,14} spin-Hall devices,¹⁵ and spin qubits.^{16,17}

Here, we consider a SiGe-based heterostructure with a compressively strained Ge quantum well (QW) at its surface. This differs from previous studies where buried Ge QWs were investigated.^{9,18,19} Despite a considerable detrimental effect on mobility, having the Ge well at the surface does present some advantages and opportunities: it allows for more conventional MOSFET-type device structures where, in principle, we can expect to achieve larger electric fields perpendicular to the Ge well and, as a result, higher charge densities, and stronger spin-orbit coupling; it should enable the fabrication of quantum-dot nanostructures with stronger charge confinement and larger level spacing; finally, it will facilitate the development of high-transparency superconducting contacts, thereby opening a new route toward Ge-based superconductor-semiconductor devices, such as Josephson field-effect transistors,^{20,21} gatemons,^{22,23} and, possibly, hybrid devices for topologically protected quantum bits based on Majorana fermions or parafermions.^{21,24}

The strained SiGe heterostructure was grown on a 200 mm Si(001) substrate by means of reduced pressure chemical vapor deposition (RP-CVD). Growth was realized using an industrial-type, mass-production system (ASM Epsilon 2000 RP-CVD), which is a horizontal, cold-wall, single wafer, load-lock reactor with a lamp-heated graphite susceptor in a quartz tube. RP-CVD offers the major advantage of unprecedented wafer scalability and is nowadays routinely used by leading companies in the semiconductor industry to grow epitaxial layers on Si wafers of up to 300 mm diameter. The heterostructures, shown schematically in Fig. 1(a), consist of a 3 μ m thick reverse linearly graded, fully relaxed Si_{0.2}Ge_{0.8}/Ge/Si(001) virtual substrate with a 32-nm-thick strained Ge QW surface layer. This is a typical design for surface channel structures employed in modern MOSFET devices. The full structure was grown in a single process without any external treatment. The surface of the Si wafers was cleaned by an *in situ* thermal bake in H₂ ambient at high temperature, above 1000 °C. The Ge epilayer was grown from a commercially available and widely used germane (GeH₄) gas precursor at a relatively low substrate temperature (<450 °C), as it is known that the growth temperature of the compressively strained Ge epilayers has to be sufficiently low to suppress surface roughening and retain compressive strain in the epilayers. Further details of material growth and characterization are described elsewhere.²⁵ The same epitaxial growth technology resulted in the creation of strained Ge QW heterostructures with superior low- and room-temperature electronic properties^{26,27} enabling the observation of various quantum phenomena including fractional quantum Hall effects,²⁸ mesoscopic effects due to spin-orbit interactions,^{2,9,18,29} and terahertz quantum Hall effects.³⁰

The studied devices have a Hall-bar geometry defined by a top-gate electrode operated in the accumulation mode [Fig. 1(b)]. Due to the absence of intentional doping, the Ge QW

^{a)} Author to whom correspondence should be addressed: silvano.defranceschi@cea.fr

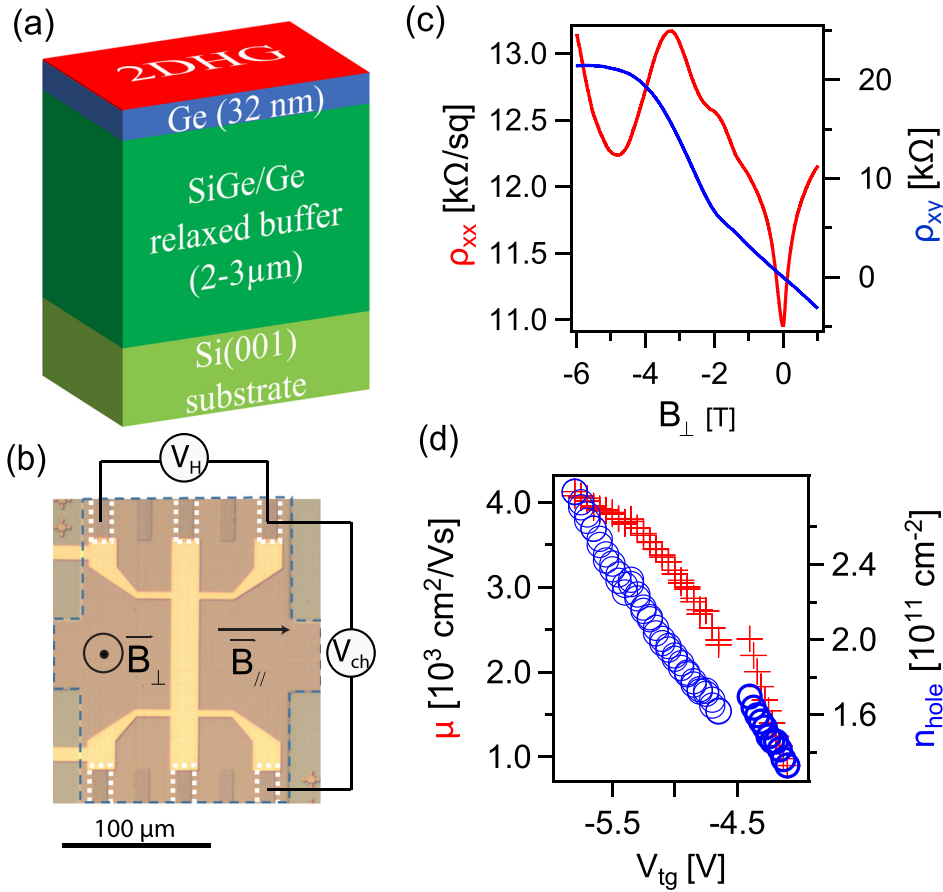


FIG. 1. (a) Schematic of the heterostructure. (b) Optical image of the Hall bar devices. The blue line highlights the mesa and the white dotted lines the Pt contacts. We measure the transverse Hall voltage (V_H) and the longitudinal channel voltage (V_{ch}) from which we extract Hall resistivity and channel resistivity, respectively. The directions of the applied fields B_{\perp} and B_{\parallel} are also indicated. (c) Channel resistivity ρ_{xx} (red) and Hall resistivity ρ_{xy} (blue) as a function of the out of plane magnetic field at $V_{tg} = -4.8$ V. Channel resistivity shows a dip at a low field, which is a signature of weak anti-localization. (d) Mobility μ (red) and carrier density n_{hole} (blue) as a function of accumulation gate voltage V_{tg} . Data points above and below $V_{tg} = -4.5$ V refer to two distinct experimental runs.

contains no carrier at low temperature. Only by applying a sufficiently negative top-gate voltage, V_{tg} , the accumulation of a two-dimensional electron gas (2DHG) can be induced in the Ge QW. Device fabrication involves the following steps: a relatively large (tens of microns wide), 55-nm-thick mesa structure is initially defined by optical lithography and dry etching in a Cl_2 plasma; ohmic contacts are successively fabricated using optical lithography, followed by Ar etching (to remove the residual oxide) and Pt deposition in an e-beam evaporator system; 30 nm of Al_2O_3 is deposited everywhere using atomic layer deposition at 250 °C; finally, the Hall-bar-shaped top gate accumulation electrode is defined by e-beam lithography and deposition of 60 nm of Ti/Au.

Magneto-transport measurements were performed in a ^3He cryostat with a base temperature of 300 mK. In the first set of experimental runs, longitudinal (ρ_{xx}) and Hall (ρ_{xy}) resistivities were measured as a function of the magnetic field, B_{\perp} , perpendicular to the 2DHG, and V_{tg} . The onset of hole accumulation was found to occur at $V_{tg} \approx -4$ V, slightly varying from one run to the other. Examples of $\rho_{xx}(B_{\perp})$ and $\rho_{xy}(B_{\perp})$ traces are given in Fig. 1(c). From Hall resistivity, we extracted the hole mobility (μ) and carrier density (n_{hole}) ranging from 800 to 4100 cm^2/Vs and from 1.3 to $2.8 \times 10^{11} \text{cm}^{-2}$, respectively [data points from two experimental runs are shown in Fig. 1(d)]. The mobility is much lower than the one reported in other strained Ge heterostructures.²⁷ This difference is likely due to the presence of charge traps at the Ge/ Al_2O_3 interface.

Following basic Hall-effect characterization, we now turn to a more in-depth investigation of the magneto-

transport properties. In Fig. 1(c), the longitudinal resistivity (red trace) exhibits a pronounced dip at zero magnetic field. Such a dip is a characteristic signature of weak anti-localization (WAL), a mesoscopic phenomenon associated with spin-orbit coupling.³¹ At zero magnetic field, the latter leads to a reduced backscattering resulting in a resistivity minimum. This quantum interference effect is suppressed by a magnetic field perpendicular to the 2DHG, accounting for the observed resistivity dip at $B_{\perp} = 0$.

This phenomenon is further investigated as shown in Fig. 2(a), where the longitudinal conductivity is now plotted as a function of B_{\perp} and for a range of V_{tg} values, after having removed the feature-less back-ground contribution from classical Drude conductivity. As a matter of fact, $\Delta\sigma_{WAL}$ represents the quantum correction resulting from WAL. Interestingly, this data set shows that the WAL peak develops and broadens upon increasing V_{tg} and, correspondingly, the perpendicular electric field and the hole density n_{hole} in the QW. All over the n_{hole} range spanned, the 2DHG occupies the first subband only, as confirmed by self-consistent tight-binding (TB) calculations.³² Figure 2(b) shows the valence-band profile calculated for $n_{hole} = 1.5 \times 10^{11} \text{cm}^{-2}$, as well as a representation of the first two hole subbands. From the in-plane dispersion of the first subband (not shown), we obtain an in-plane effective mass $m^* = 0.07m_0$, where m_0 is the bare electron mass. This value is slightly smaller, yet close, to those reported in previous studies on buried Ge QWs.^{9,18,33,34}

The evolution of the WAL peak in Fig. 2(a) suggests that the underlying spin-orbit coupling is gate tunable. We

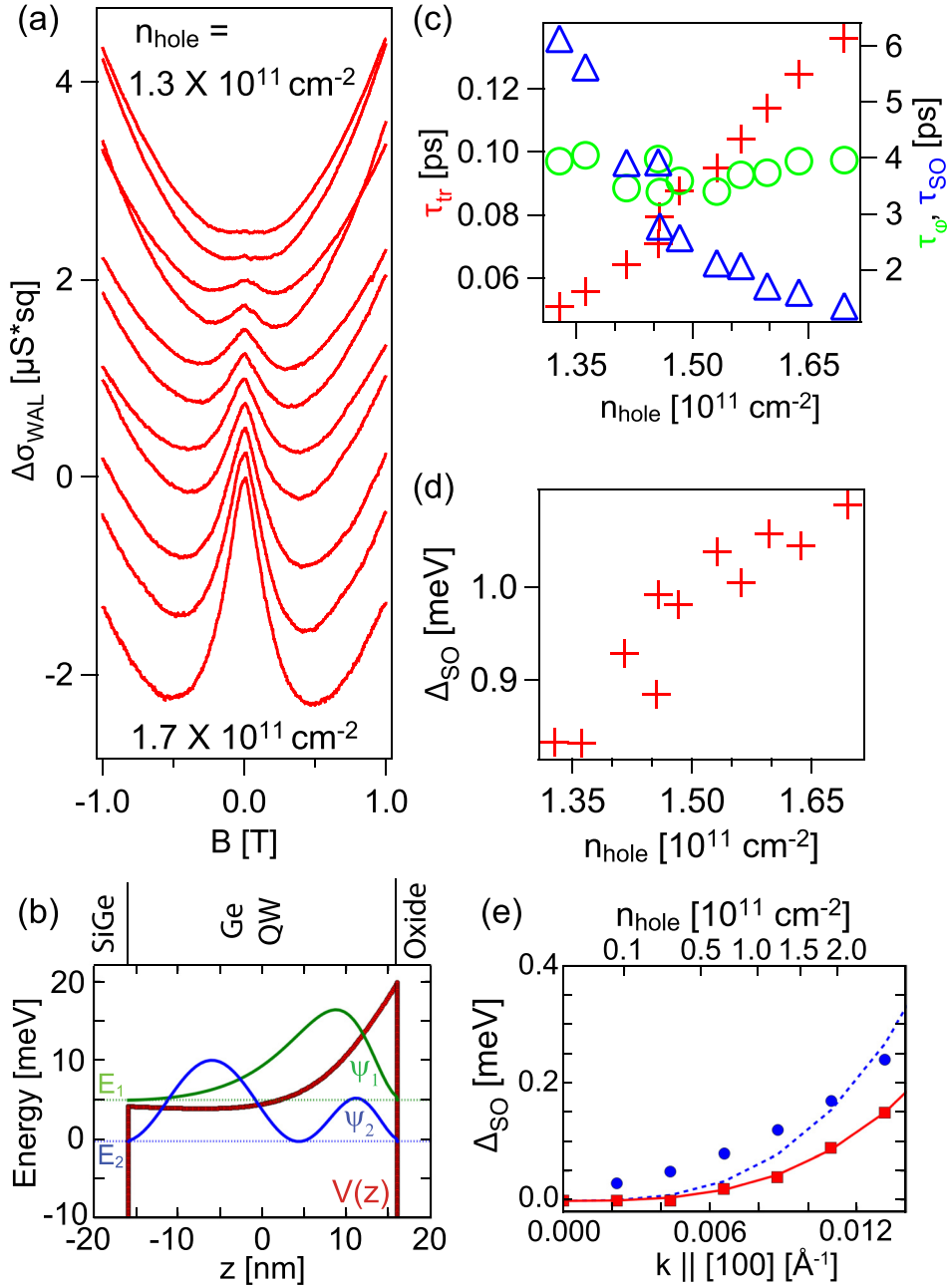


FIG. 2. (a) Traces of the weak anti-localization contribution to the channel conductivity $\Delta\sigma_{WAL}$ as a function of B_\perp for different accumulation gate voltages and carrier densities from $1.3 \times 10^{11} \text{ cm}^{-2}$ (top trace) to $1.7 \times 10^{11} \text{ cm}^{-2}$ (bottom trace, traces are offset for better visibility). The weak anti-localization peaks emerge as carrier density is increased. (b) Valence band diagram and squared wave functions of the first two hole subbands calculated for $n_{hole} = 1.5 \times 10^{11} \text{ cm}^{-2}$. The Fermi energy is $E_F = 0$. (c) Evolution of scattering time τ_{tr} (red crosses), phase relaxation time τ_ϕ (green circles), and spin relaxation time τ_{SO} (blue triangles) as a function of carrier density. (d) Evolution of the spin splitting energy Δ_{SO} as a function of carrier density. (e) Spin splitting energy calculated with a TB model, with and without interface roughness (squares and circles) and fits to $\Delta_{SO} = \alpha_3 E_\perp k_{||}^3$ (solid and dotted lines, respectively). To simulate the interface roughness, we used a Gaussian auto-correlation function model, with root-mean-square fluctuation $\Delta = 0.2 \text{ nm}$ and correlation length $\Lambda = 1.0 \text{ nm}$. In this case, the fit reproduces well the TB calculation with $\alpha_3 E_\perp \approx 73 \text{ eV \AA}^3$ and $\alpha_3 \approx 5 \times 10^5 \text{ e \AA}^4$.

expect it to be of a Rashba-type since Dresselhaus spin-orbit coupling terms should be negligible due to the existence of bulk inversion symmetry in the Ge QW and surface roughness.³⁵ The WAL peak can be fitted to the formula³⁶

$$\Delta\sigma_{WAL}(B_\perp) = \frac{e^2}{2\pi^2\hbar} \left\{ \Psi\left(\frac{1}{2} + \frac{B_\phi}{B_\perp} + \frac{B_{SO}}{B_\perp}\right) + \frac{1}{2}\Psi\left(\frac{1}{2} + \frac{B_\phi}{B_\perp} + 2\frac{B_{SO}}{B_\perp}\right) - \frac{1}{2}\Psi\left(\frac{1}{2} + \frac{B_\phi}{B_\perp}\right) - \ln\left(\frac{B_\phi}{B_\perp} + \frac{B_{SO}}{B_\perp}\right) - \frac{1}{2}\ln\left(\frac{B_\phi}{B_\perp} + \frac{2B_{SO}}{B_\perp}\right) + \frac{1}{2}\ln\left(\frac{B_\phi}{B_\perp}\right) \right\}, \quad (1)$$

where $\Psi(X)$ is the digamma function, B_ϕ is the phase coherence field, and B_{SO} is the characteristic field associated with the Rashba spin orbit coupling. From the fitting parameters

B_ϕ and B_{SO} , we can extract the phase coherence time τ_ϕ and the spin relaxation time τ_{SO} with $\tau_i = m^*/4\pi\hbar\mu n_{hole} B_i$, i being either ϕ or SO . We note that the large width of the observed WAL peak is consistent with the relatively small values obtained for the scattering time ($\tau_{tr} = m^*\mu/e$).

These values, as well as those for τ_ϕ , τ_{SO} are displayed as a function of carrier density in Fig. 2(c). The evolution of these characteristic time scales with respect to n_{hole} provides a hint on the underlying mechanism for spin relaxation. If spin relaxation was due to impurity scattering (Elliott-Yafet mechanism^{37,38}), then τ_{SO} should increase with τ_{tr} and decrease with the carrier density ($\tau_{SO} \propto \tau_{tr}/n_{hole}^2$). This does not correspond to the observed trend. On the other hand, if spin relaxation occurred in between scattering events, due to spin-orbit-induced rotation (Dyakonov-Perel mechanism³⁹), the spin relaxation time should decrease with τ_{tr} and with the spin splitting energy Δ_{SO} ($\tau_{SO} \propto 1/(\tau_{tr} \times \Delta_{SO}^2)$). Our experimental finding is consistent with this second scenario, which allows us to

deduce the spin splitting energy, $\Delta_{SO} \sim \hbar(2\tau_{so}\tau_{tr})^{-1/2}$, and its dependence on n_{hole} [see Fig. 2(d)]. The obtained values of Δ_{SO} are around 1 meV, i.e., a few times larger but still comparable to those reported for similar heterostructures and different experimental methods.^{9,18,19}

In our strained-Ge QW system, where the 2DHG has a predominantly heavy-hole character, we expect the Rashba spin-orbit coupling to be dominated by a cubic term in the in-plane momentum, $k_{||}$, as also reported in previous studies.^{9,18,19,40} Figure 2(e) shows a self-consistent TB calculation of $\Delta_{SO}(k_{||})$ in a 32-nm thick Ge film saturated by hydrogen atoms.³² We note that the linear $\propto k_{||}$ dependence at small $k_{||}$ is quickly overcome by a $\propto k_{||}^3$ dependence. Interestingly, our calculation shows that for a rough, lower symmetry film, the linear component is almost suppressed (it oscillates rapidly with the film thickness and is averaged down to ~ 0 by surface roughness). The calculated values of Δ_{SO} appear to be an order of magnitude lower than the experimental values reported in Fig. 2(d). This discrepancy may be ascribed to the simplified description of the surface in the TB calculation, the magnitude of Δ_{SO} being very sensitive to boundary conditions.

To further investigate the nature of the zero-field conductivity enhancement, magneto-transport measurements were performed also with the magnetic field applied in the plane of the 2DHG, as indicated in Fig. 3. For first order, an in-plane magnetic field is not expected to break the WAL effect because it produces no flux through the time-reversed back-scattering trajectories. Contrary to this expectation, the longitudinal conductivity measured as a function of the in-plane magnetic field, $B_{||}$, does exhibit a clear zero-field peak with a characteristic half width at half maximum of ~ 0.7 T, i.e., several times larger than in the case of the perpendicular field.

We can rule out the possibility of a misalignment of the magnetic field with respect to the plane of the 2DHG. In fact, from a simultaneous measurement of the Hall resistivity, also shown in Fig. 3, we estimate a misalignment of 2° . Therefore, the out-of-plane component of the applied field is far too small to explain the observed WAL peak.

Instead, following Minkov *et al.*,⁴¹ the effect can be ascribed to an effective finite thickness of the 2DHG, and the WAL peak in magneto-conductivity can be expressed as

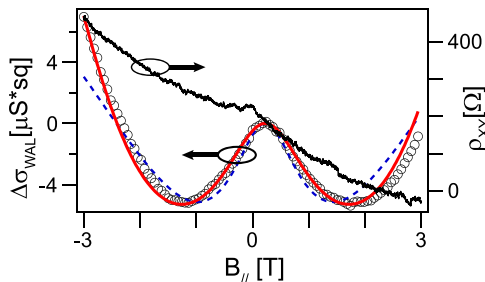


FIG. 3. Black trace: Hall resistivity ρ_{xy} as a function of the in-plane magnetic field at $V_{tg} = -5.8$ V. The small dependence on field results from a small perpendicular field component. We estimate an angle of only 2° between $B_{||}$ and the chip plane. Black circles: quantum correction to channel conductivity $\Delta\sigma_{WAL}$, revealing a weak anti-localization peak. The blue dashed line and the red solid line are fits to the model from Minkov *et al.*⁴¹ without and with the addition of a $B_{||}^6$ term, respectively.

$$\Delta\sigma_{WAL}(B_{||}) = \frac{e^2}{4\pi^2\hbar} \left[2\ln\left(\frac{B_\phi + B_{SO} + \Delta_r}{B_\phi + B_{SO}}\right) + \ln\left(\frac{B_\phi + 2B_{SO} + \Delta_r}{B_\phi + 2B_{SO}}\right) - \ln\left(\frac{B_\phi + \Delta_r + \Delta_s}{B_\phi}\right) + S\left(\frac{B_\phi + \Delta_r}{B_{SO}}\right) - S\left(\frac{B_\phi}{B_{SO}}\right) \right], \quad (2)$$

where Δ_r and Δ_s are $B_{||}$ -dependent corrections to B_ϕ taking into account the effect of surface roughness and Zeeman splitting, respectively. Following Ref. 41, we assume $\Delta_r = rB_{||}^2$ and $\Delta_s = sB_{||}^2$. The $S(x)$ function in Eq. (2) can be explicitly written as

$$S(x) = \frac{8}{\sqrt{7+16x}} \left[\arctan\left(\frac{\sqrt{7+16x}}{1-2x}\right) - \pi\Theta(1-2x) \right], \quad (3)$$

where Θ is the Heaviside step function. For the effective fields B_{SO} and B_ϕ , we take the values extracted from the previously discussed magneto-transport measurements in the perpendicular magnetic field, for the same carrier density, i.e., $B_{SO} = 170$ mT and $B_\phi = 19$ mT.

The dotted blue line in Fig. 3 is a fit to Eq. (2) using the proportionality factors r and s as fitting parameters. The fit shows only moderate agreement with the data. An improved fit can be obtained by introducing in the expression of Δ_r a second orbital term proportional to $B_{||}^6$, i.e., $\Delta_r = r \times B_{||}^6 + q \times B_{||}^6$, with the additional fitting parameter q . This second term describes $B_{||}$ -induced time-reversal symmetry breaking via the virtual occupation of higher energy subbands.⁴²⁻⁴⁴ The new fit, shown by a solid red line in Fig. 3, is in remarkably good agreement with the experimental data set over the entire $B_{||}$ range. Following Ref. 43, the value of the fit parameter q can be related to the effective thickness d of the 2DHG, i.e., $d \sim (q\Phi_0^5/4\pi^2n_{hole}^2)^{1/14}$. We find a realistic $d \sim 14$ nm, which can be regarded as a sanity check for the model used.

The authors would like to thank M. Houzet, J. Meyer, S. Oda, and M. Sanquer for fruitful discussions. We acknowledge financial support from the Agence Nationale de la Recherche, through the TOPONANO project, from the EU through the ERC Grant No. 280043, and from the Fondation Nanosciences, Grenoble.

¹F. A. Zwanenburg, A. S. Dzurak, A. Morello, M. Y. Simmons, L. C. L. Hollenberg, G. Klimeck, S. Rogge, S. N. Coppersmith, and M. A. Eriksson, *Rev. Mod. Phys.* **85**, 961 (2013).

²C. Morrison and M. Myronov, *Phys. Status Solidi A* **213**, 2809 (2016).

³K. Sawano, K. Toyama, R. Masutomi, T. Okamoto, N. Usami, K. Arimoto, K. Nakagawa, and Y. Shiraki, *Appl. Phys. Lett.* **95**, 122109 (2009).

⁴C. Morrison, C. Casteleiro, D. R. Leadley, and M. Myronov, *Appl. Phys. Lett.* **109**, 102103 (2016).

⁵C. Testelin, F. Bernardot, B. Eble, and M. Chamarro, *Phys. Rev. B* **79**, 195440 (2009).

⁶H. Watzinger, C. Kloeffer, L. Vukušić, M. D. Rossell, V. Sessi, J. Kukučka, R. Kirchschrager, E. Lausacker, A. Truhlar, M. Glaser, A. Rastelli, A. Fuhrer, D. Loss, and G. Katsaros, *Nano Lett.* **16**, 6879 (2016).

⁷N. Ares, V. N. Golovach, G. Katsaros, M. Stoffel, F. Fournel, L. I. Glazman, O. G. Schmidt, and S. De Franceschi, *Phys. Rev. Lett.* **110**, 046602 (2013).

⁸C. Kloeffer, M. Trif, and D. Loss, *Phys. Rev. B* **84**, 195314 (2011).

- ⁹C. Morrison, P. Wiśniewski, S. D. Rhead, J. Foronda, D. R. Leadley, and M. Myronov, *Appl. Phys. Lett.* **105**, 182401 (2014).
- ¹⁰A. Zarassi, Z. Su, J. Danon, J. Schwenderling, M. Hovevar, B.-M. Nguyen, J. Yoo, S. A. Dayeh, and S. M. Frolov, "Magnetic field evolution of spin blockade in Ge/Si nanowire double quantum dots," *Phys. Rev. B* **95**, 155416 (2017).
- ¹¹N. Ares, G. Katsaros, V. N. Golovach, J. J. Zhang, A. Prager, L. I. Glazman, O. G. Schmidt, and S. D. Franceschi, *Appl. Phys. Lett.* **103**, 263113 (2013).
- ¹²V. N. Golovach, M. Borhani, and D. Loss, *Phys. Rev. B* **74**, 165319 (2006).
- ¹³S. Datta and B. Das, *Appl. Phys. Lett.* **56**, 665 (1990).
- ¹⁴D. D. Awschalom and M. E. Flatté, *Nat. Phys.* **3**, 153 (2007).
- ¹⁵T. Jungwirth, J. Wunderlich, and K. Olejník, *Nat. Mater.* **11**, 382 (2012).
- ¹⁶K. C. Nowack, F. H. L. Koppens, Y. V. Nazarov, and L. M. K. Vandersypen, *Science* **318**, 1430 (2007).
- ¹⁷R. Maurand, X. Jehl, D. Kotekar-Patil, A. Corna, H. Bohuslavskiy, R. Laviéville, L. Hutin, S. Barraud, M. Vinet, and M. Sanquer, *Nat. Commun.* **7**, 13575 (2016).
- ¹⁸M. Failla, M. Myronov, C. Morrison, D. Leadley, and J. Lloyd-Hughes, *Phys. Rev. B* **92**, 045303 (2015).
- ¹⁹R. Moriya, K. Sawano, Y. Hoshi, S. Masubuchi, Y. Shiraki, A. Wild, C. Neumann, G. Abstreiter, D. Bougeard, T. Koga, and T. Machida, *Phys. Rev. Lett.* **113**, 086601 (2014).
- ²⁰J. Xiang, A. Vidan, M. Tinkham, R. M. Westervelt, and C. M. Lieber, *Nat. Nanotechnol.* **1**, 208 (2006).
- ²¹Z. Su, A. Zarassi, B.-M. Nguyen, J. Yoo, S. A. Dayeh, and S. M. Frolov, "High critical magnetic field superconducting contacts to Ge/Si core/shell nanowires," preprint [arXiv:1610.03010](https://arxiv.org/abs/1610.03010) (2016).
- ²²G. de Lange, B. van Heck, A. Bruno, D. J. van Woerkom, A. Geresdi, S. R. Plissard, E. P. A. M. Bakkers, A. R. Akhmerov, and L. DiCarlo, *Phys. Rev. Lett.* **115**, 127002 (2015).
- ²³L. Casparis, T. W. Larsen, M. S. Olsen, F. Kuemmeth, P. Krogstrup, J. Nygård, K. Petersson, and C. M. Marcus, *Phys. Rev. Lett.* **116**, 150505 (2016).
- ²⁴F. Maier, J. Klinovaja, and D. Loss, *Phys. Rev. B* **90**, 195421 (2014).
- ²⁵M. Myronov, A. Dobbie, V. A. Shah, X.-C. Liu, V. H. Nguyen, and D. R. Leadley, *Electrochem. Solid-State Lett.* **13**, H388 (2010).
- ²⁶A. Dobbie, M. Myronov, R. J. H. Morris, A. H. A. Hassan, M. J. Prest, V. A. Shah, E. H. C. Parker, T. E. Whall, and D. R. Leadley, *Appl. Phys. Lett.* **101**, 172108 (2012).
- ²⁷M. Myronov, C. Morrison, J. Halpin, S. Rhead, C. Casteleiro, J. Foronda, V. A. Shah, and D. Leadley, *Jpn. J. Appl. Phys., Part 1* **53**, 04EH02 (2014).
- ²⁸Q. Shi, M. A. Zudov, C. Morrison, and M. Myronov, *Phys. Rev. B* **91**, 241303 (2015).
- ²⁹J. Foronda, C. Morrison, J. E. Halpin, S. D. Rhead, and M. Myronov, *J. Phys.: Condens. Matter* **27**, 022201 (2015).
- ³⁰M. Failla, J. Keller, G. Scalari, C. Maissen, J. Faist, C. Reichl, W. Wegscheider, O. J. Newell, D. R. Leadley, M. Myronov, and J. Lloyd-Hughes, *New J. Phys.* **18**, 113036 (2016).
- ³¹W. Knap, C. Skierbiszewski, A. Zduniak, E. Litwin-Staszewska, D. Bertho, F. Kobbi, J. L. Robert, G. E. Pikus, F. G. Pikus, S. V. Iordanskii, V. Mosser, K. Zekentes, and Y. B. Lyanda-Geller, *Phys. Rev. B* **53**, 3912 (1996).
- ³²Y. M. Niquet, D. Rideau, C. Tavernier, H. Jaouen, and X. Blase, *Phys. Rev. B* **79**, 245201 (2009).
- ³³M. A. Zudov, O. A. Mironov, Q. A. Ebner, P. D. Martin, Q. Shi, and D. R. Leadley, *Phys. Rev. B* **89**, 125401 (2014).
- ³⁴D. Laroche, S.-H. Huang, Y. Chuang, J.-Y. Li, C. W. Liu, and T. M. Lu, *Appl. Phys. Lett.* **108**, 233504 (2016).
- ³⁵L. E. Golub and E. L. Ivchenko, *Phys. Rev. B* **69**, 115333 (2004).
- ³⁶S. Iordanskii, Y. B. Lyanda-Geller, and G. Pikus, *ZhETF Pisma Redaktsiiu* **60**, 199 (1994).
- ³⁷R. J. Elliott, *Phys. Rev.* **96**, 266 (1954).
- ³⁸Y. Yafet, *Phys. Lett. A* **98**, 287 (1983).
- ³⁹M. Dyakonov and V. Perel, *Sov. Phys. Solid State, USSR* **13**, 3023 (1972).
- ⁴⁰R. Winkler, D. Culcer, S. J. Papadakis, B. Habib, and M. Shayegan, *Semicond. Sci. Technol.* **23**, 114017 (2008).
- ⁴¹G. Minkov, A. Germanenko, O. Rut, A. Sherstobitov, L. Golub, B. Zvonkov, and M. Willander, *Phys. Rev. B* **70**, 155323 (2004).
- ⁴²V. I. Fal'ko, *J. Phys.: Condens. Matter* **2**, 3797 (1990).
- ⁴³J. S. Meyer, A. Altland, and B. L. Altshuler, *Phys. Rev. Lett.* **89**, 206601 (2002).
- ⁴⁴D. M. Zumbühl, J. B. Miller, C. M. Marcus, K. Campman, and A. C. Gossard, *Phys. Rev. Lett.* **89**, 276803 (2002).